Progress In Electromagnetics Research B, Vol. 98, 39–57, 2023

Coupling Coefficient Calculation of Arbitrarily Positioned Rectangular Coils with Double Magnetic Shielding in Wireless Power Transfer Systems

Zhongqi Li[1, 2, *], Zhongbang Chen[1], Jing Li[1, 3], Huadong Liu[4], and Qing Huang[5]

Abstract—Coupling coefficient is a key parameter for the coil design of wireless power transfer (WPT) systems. The accurate calculation of coupling coefficient is an important theoretical basis for optimizing the coil structure and improving the transmission efficiency in WPT systems. In this paper, the magnetic flux density distribution of rectangular spiral coils with double magnetic shielding is studied, and an analytical model of coupling coefficient between arbitrarily positioned rectangular spiral coils is established. First, the incident magnetic flux density is obtained based on the dual Fourier transformation and the relationship between the magnetic flux density and magnetic vector potential. Second, the reflected magnetic flux density in the region of the receiving coil is solved by using Poisson's equation, Laplace's equation, and boundary conditions. Finally, the formula for the coupling coefficient between rectangular spiral coils is derived by the spatial frame transformation method and integral method. The calculation results agree well with the finite element simulation value and experimental measurements, which verifies the correctness of the calculation formula of the coupling coefficient.

1. INTRODUCTION

Wireless power transfer (WPT) is a transfer method in which electrical energy is transmitted from the power source to load without contact [1–3], including inductive-coupling-power transfer, microwave power transfer, laser-power transfer, etc. [4]. It greatly improves the flexibility and safety of devices, avoiding abrasion, spark, and electric leakage of the traditional contact power supply [5, 6]. Therefore, WPT technology has broad application prospects in the fields of electric vehicles [7–9], rail transit [10], implantable therapy [11, 12], petroleum exploitation, marine science [13, 14], smart home, and consumer electronics [15]. However, coupling coefficient between the transmitting coil and receiving coil is variable with their positions in actual applications, which leads to the unstable transmission efficiency and output power of the system. Thus, it is of great significance to study the coupling coefficient of arbitrarily positioned coils.

With the further development of WPT technology and the expansion of application fields, higher requirements have been put forward for both the power transmission efficiency and magnetic shielding performance of WPT systems [16]. According to the characteristics of the WPT system, ferrite or aluminum is often used as the shielding material. Compared with ferrite, aluminum has a better performance on shielding magnetic fields but reduces the coupling coefficient between coils [17–19]. To compensate for the defect of the single material shielding, the coupling coefficient between coils with double shielding (a shielding structure that consists of two magnetic shielding substrates of different

---

Received 8 September 2022, Accepted 20 December 2022, Scheduled 4 January 2023

* Corresponding author: Zhongqi Li (my3eee@126.com).

[1] College of Transportation Engineering, Hunan University of Technology, Zhuzhou, Hunan 412007, China. [2] College of Electrical and Information Engineering, Hunan University, Changsha, Hunan 412008, China. [3] School of Electrical Engineering, Southwest Jiaotong University, Chengdu, Sichuan 611730, China. [4] CRRC Zhuzhou Institute Co., LTD., Zhuzhou 412007, China. [5] Hunan Electric Car Special Equipment Co., Ltd., Zhuzhou 412007, China.

materials) is studied. At present, the coils used in WPT systems are mainly circular and rectangular. The research results of the coupling coefficient calculation method for circular coils [20, 21] are relatively plentiful; however, research on the coupling coefficient calculation for the rectangular coil, especially for the rectangular coil with the magnetic shielding, is still novel and scarce [22].

In terms of the coupling coefficient calculation for rectangular coils in air, the coupling coefficient between two coaxial rectangular coils is calculated according to Neumann's formula in [23]. Ref. [24] uses the quadrupole superposition method to predict the inductances of coils with horizontal misalignment. In [25], a magnetic field analysis method based on the Biot-Savart law is obtained which considers horizontal misalignment and vertical angular misalignment. On this basis, the mutual inductance of the coils is calculated for all possible variations, including lateral and angular misalignments, in [26]. In addition, in [27], the analytical calculation formula of the mutual inductance between two arbitrarily positioned rectangular filaments is proposed based on the calculation expression of the mutual inductance between two arbitrarily positioned straight filaments. According to Neumann's formula, the general expression of mutual inductance for two polygon coils at arbitrary positions is deduced [28].

In terms of the coupling coefficient calculation for rectangular coils with magnetic shielding, an analytical solution for the eddy current distribution of a rectangular coil arranged parallel to a conducting slab is derived by solving Maxwell's equations in [29]. Based on the second-order vector potential, the magnetic flux density distribution generated by eddy currents in the conductor is calculated, and the impedance analysis expression of the rectangular coil is then obtained in [30]. In [31], the magnetic field model of a rectangular coil with a magnetic shielding is described with the dual Fourier series and is obtained by combining the magnetic vector and scalar potentials. In addition, the mutual inductance of rectangular planar spiral coils between two substrates is calculated based on the Fourier-Bessel transformation and dual Fourier transformation in [32]. Reference [33] presents analytical modeling for the mutual inductance between noncoaxial rectangular coils with shielding, which involves Fourier analysis, magnetic vectors, and scalar potential definitions. To the best of our knowledge, the coupling coefficient calculation method for arbitrarily positioned rectangular coils with double magnetic shielding has not been reported in previous literature.

In this paper, a generalized theory based on magnetic flux density and spatial frame transformation method is presented with the coupling coefficient calculation method between the transmitting and receiving coils arbitrarily positioned on a double-layer shielding substrate. Using the proposed formula, the coupling coefficient between the arbitrarily positioned rectangular coils above a double-layer shielding is obtained without the time-consuming finite element analysis (FEA) method.

The remainder of the paper is organized as follows. A calculation formula of the coupling coefficient between arbitrarily positioned rectangular coils with a double-layer magnetic shielding is obtained in Section 1. Section 2 shows the FEA simulation model and experimental setup, and the simulation errors and experiment errors for various misalignments are also discussed. Finally, some conclusions are drawn in Section 3.

2. COUPLING COEFFICIENT CALCULATION

In this section, a spatial frame transformation method is proposed to obtain the magnetic flux density in different frames, which reflects the relationship between the coordinates of the same point in different frames. An analytical model of coupling coefficient for arbitrarily positioned rectangular plane spiral coils with double magnetic shielding is established by this method. Analysis flowchart of the coupling coefficient is as shown in Fig. 1.

2.1. Common Position Variations of Rectangular Coils

The coupling coefficient between two coils changes with their relative position. When the receiving coil is parallel and close to the transmitting coil, the flux linkage is larger, and the coupling coefficient is also larger. When the receiving coil is perpendicular to and away from the transmitting coil, the coupling between these coils is weakened, and the coupling coefficient is reduced. However, the misalignment of the receiving and transmitting coils is unavoidable in practical applications. To obtain a practical

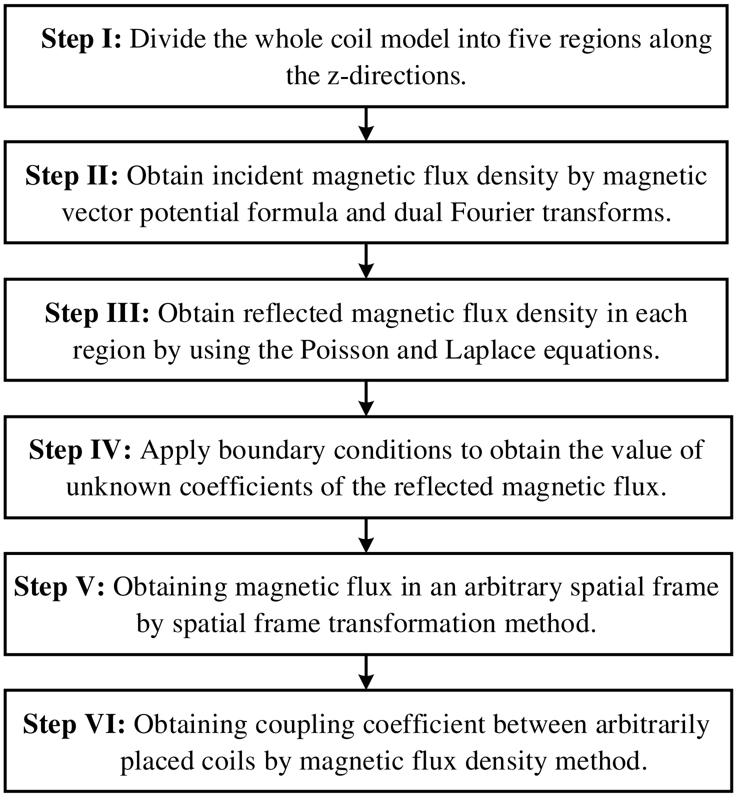

Figure 1. Flow chart of the coupling coefficient calculation.

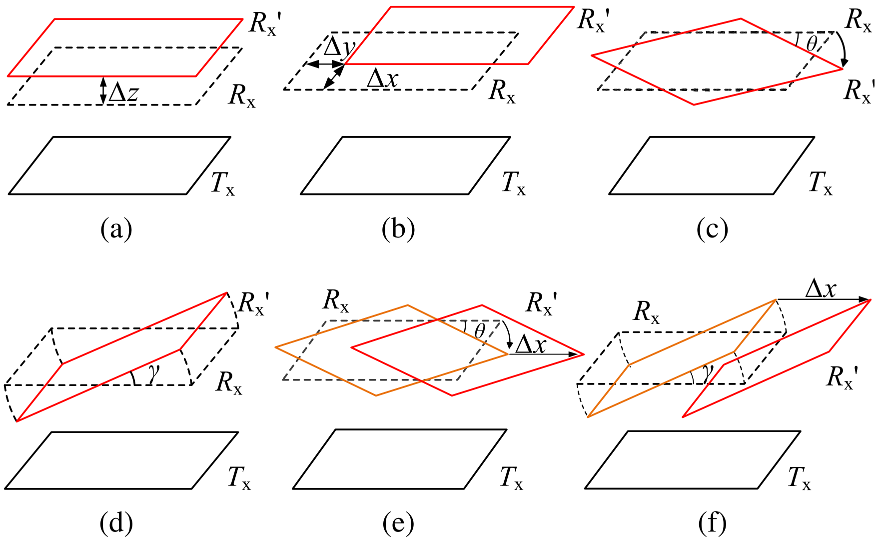

Figure 2. Schematic of general position changes for coils, (a) vertical distance variation, (b) horizontal misalignment, (c) horizontal angular misalignment, (d) vertical angular misalignment, (e) both horizontal angular and horizontal misalignment, (f) both vertical angular and horizontal misalignment.

calculation formula for the coupling coefficient between the rectangular coils, the main position changes of the rectangular coil are analyzed, and the position change diagram is shown in Fig. 2.

As shown in Fig. 2, T_x is the transmitting coil, and R_x and R'_x are the receiving coils before and after the position change, respectively. The symmetric distribution means that T_x is coaxial to R'_x, and there is no horizontal angular misalignment, such as vertical misalignment, as shown in Fig. 2(a). Figs. 2(b)–(f) show an asymmetrical distribution, which includes horizontal misalignment, angular misalignment, and both horizontal and angular misalignments. Parameters of the position change of the rectangular coil are described in Table 1.

Table 1. Parameters of coils position variation.

Symbol	Description
Δx	Distance variation along the X-axis
Δy	Distance variation along the Y-axis
Δz	Distance variation along the Z-axis
ψ	Angle of the frame around the X-axis
γ	Angle of the frame around the Y-axis
θ	Angle of the frame around the Z-axis

2.2. Expression of Magnetic Flux Density

In this model, the magnetic flux density consists of incident magnetic flux density B_i and reflected flux density B_r. The incident magnetic flux density B_i is excited by a harmonic current through the transmitting coil, and the reflected flux density B_r is generated by the eddy current in the magnetic shielding. The schematic diagram of rectangular coils with double magnetic shielding is shown in Fig. 3. The whole model is divided into five regions: Regions 2 and Region 3 are two limited thickness substrates that represent the magnetic shielding material placed under the coils, and the rest of the regions are in air. The upper surface of the magnetic shielding material coincides with $z = 0$ plane; s_1 is the height of T_x; s_2 is the height of R_x. μ_i, σ_i, and t_i $(i = 2, 3)$ are the relative permeability, conductivity, and thickness of the substrate, respectively. a_1 and a_2 are half length and half width of T_x, and b_1 and b_2 are half length and half width of R_x. It is generally believed that only the reflected magnetic flux density B_r exists in Regions 1–3, while Regions 4 and 5 contain both reflected magnetic flux density B_r and magnetic incident flux density B_i.

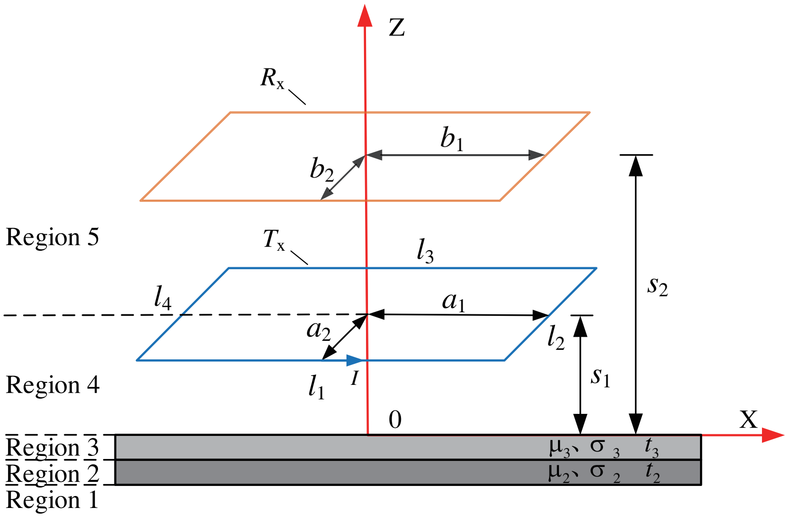

Figure 3. Rectangular coils with double magnetic shields.

2.2.1. *Incident Magnetic Flux Density*

The transmitting coil drives a current, and the magnetic incident flux density B_i around the transmitting coil is as follows [34]:

$$B_i = \nabla \times A \tag{1}$$

where A is the magnetic vector potential, and $\nabla \times A$ represents the curl of A.

The magnetic vector potential of point $P(x,\, y,\, z)$ is as follows [35]:

$$A\left(x,y,z\right) = \frac{\mu_0}{4\pi}\int_v \frac{J\left(x',y',z'\right)dv'}{R} \tag{2}$$

where J is the current density, v the current distribution of the transmitting coil, and R the distance from $P(x,\, y,\, z)$ to source point $(x',\, y',\, z')$.

Dual Fourier transforms are used to solve (2) as follows:

$$b\left(\xi,\eta,z\right) = \int_{-\infty}^{\infty}\int_{-\infty}^{\infty} B\left(x,y,z\right)e^{-j(x\xi+y\eta)}dxdy \tag{3}$$

$$B\left(x,y,z\right) = \frac{1}{4\pi^2}\int_{-\infty}^{\infty}\int_{-\infty}^{\infty} b\left(\xi,\eta,z\right)e^{j(x\xi+y\eta)}d\xi d\eta \tag{4}$$

where ξ and η are dual Fourier integral variables.

Substituting (1) and (2) into (3), (5) and (6) can be obtained as follows:

$$\begin{cases} b_{ix} = -j\eta a_z - \dfrac{\partial a_y}{\partial z} \\ b_{iy} = \dfrac{\partial a_x}{\partial z} + j\xi a_z \\ b_{iz} = -j\xi a_y + j\eta a_x \end{cases} \tag{5}$$

$$a\left(\xi,\eta,z\right) = \frac{\mu_0}{2}\int_v \frac{1}{k}e^{-j(x'\xi+y'\eta)}J\left(x',y',z'\right)e^{-k|z-s_1|}dv' \tag{6}$$

where a_x, a_y, a_z, b_{ix}, b_{iy}, and b_{iz} are the X-axis, Y-axis, and Z-axis components of the magnetic vector potential and incident magnetic flux density, respectively, and $k = \sqrt{\xi^2+\eta^2}$.

Taking into account the current distribution of T_x in Fig. 3, the incident magnetic flux density in Regions 5 can be expressed as (7)–(9).

$$b_{5ix} = \frac{2\mu_0 I \sin\left(\xi a_1\right)\sin\left(\eta a_2\right)}{j\eta}\, e^{(s_1-z)k} = C_{5ix}e^{-kz} \tag{7}$$

$$b_{5iy} = \frac{2\mu_0 I \sin\left(\xi a_1\right)\sin\left(\eta a_2\right)}{j\eta}\, e^{(s_1-z)k} = C_{5iy}e^{-kz} \tag{8}$$

$$b_{5iz} = \frac{2\mu_0 I k \sin\left(\xi a_1\right)\sin\left(\eta a_2\right)}{-\xi\eta}\, e^{(s_1-z)k} = C_{5iz}e^{-kz} \tag{9}$$

2.2.2. *Reflected Magnetic Flux Density*

According to the Maxwell's equations, the reflected magnetic flux density in regions satisfies the following equations:

$$\nabla^2 B_n - j\omega\mu_0\mu_n\sigma_n B_n = 0 \tag{10}$$

$$\nabla \cdot B_n = 0 \tag{11}$$

where ∇^2 is the Laplacian; ω is the angular frequency of power; μ_0 is the vacuum permeability; μ_n, σ_n are the relative permeability and conductivity of Region n ($n = 2$ and 3), respectively.

Substituting (10) and (11) into (3), Equations (12) and (13) can be obtained as follows:

$$\frac{\partial^2 b_n}{\partial z^2} - \left(\xi^2+\eta^2+j\omega\mu_0\mu_n\sigma_n\right)b_n = 0 \tag{12}$$

$$-j\xi b_{nx} - j\eta b_{ny} + \frac{\partial b_{nz}}{\partial z} = 0 \tag{13}$$

Taking into account that $J_{nz}=0$, $J_n = \nabla \times H_n$, and $B_n = \mu_n H_n$, the relationship between b_{nx} and b_{ny} can be obtained as follows:

$$\xi b_{ny} = \eta b_{nx} \tag{14}$$

According to (13) and (14), the relationship among b_{nx}, b_{ny}, and b_{nz} can be derived as follows:

$$b_{nx} = \frac{\xi}{jk^2}\frac{\partial b_{nz}}{\partial z} \tag{15}$$

$$b_{ny} = \frac{\eta}{jk^2}\frac{\partial b_{nz}}{\partial z} \tag{16}$$

For the second order partial differential Equation (12), the general solution is given by (17).

$$b_{nz} = C_n e^{\lambda_n z} + C'_n e^{-\lambda_n z} \tag{17}$$

where C_n and C'_n are undetermined coefficients, which can be obtained by boundary equations, $\lambda_n = \sqrt{k^2 + j\omega\mu_0\mu_n\sigma_n}$.

Considering that B_n should tend to zero when z tends to positive or negative infinity, and the reflected magnetic flux density in Region 5 can be written as follows:

$$b_{5rz} = C_{5rz}e^{-kz} \tag{18}$$

2.3. Boundary Conditions

According to the boundary conditions, the normal component of the magnetic induction intensity across the boundary between the two material regions is continuous; if there is no surface current flowing in a direction perpendicular to the tangential component of the field, then the tangential component of the magnetic field intensity is continuous across the boundary. The Z-component of B and the X-component of H can be prescribed as follows:

$$\begin{cases} b_{1z} = b_{2z},\ b_{1x} = b_{2x}/\mu_2 \quad (z=0) \\ b_{2z} = b_{3z},\ b_{2x}/\mu_2 = b_{3x}/\mu_3 \quad (z=-t_3) \\ b_{3z} = b_{4iz} + b_{4rz},\ b_{3x}/\mu_3 = b_{4ix} + b_{4rx} \quad (z=-t_3-t_2) \end{cases} \tag{19}$$

The undetermined coefficients of the reflected magnetic flux density in Region 5 can be obtained as follows by solving (19).

$$C_{5rx} = \frac{2}{j\eta}\mu_0 I \sin(\xi a_1)\sin(\eta a_2) T e^{-s_1 k} \tag{20}$$

$$C_{5ry} = \frac{2}{j\xi}\mu_0 I \sin(\xi a_1)\sin(\eta a_2) T e^{-s_1 k} \tag{21}$$

$$C_{5rz} = \frac{-2}{\xi\eta}\mu_0 I \sin(\xi a_1)\sin(\eta a_2) T e^{-s_1 k} \tag{22}$$

where

$$T = \frac{(p_1p_4e^{2\lambda_3t_3} + p_2p_3) + v(p_2p_4e^{2\lambda_3t_3} + p_1p_3)e^{-2\lambda_2t_2}}{(p_1p_3e^{2\lambda_3t_3} + p_2p_4) + v(p_2p_3e^{2\lambda_3t_3} + p_1p_4)e^{-2\lambda_2t_2}} \tag{23}$$

where $p_1 = m_3 + m_2$, $p_2 = m_3 - m_2$, $p_3 = 1 + m_3$, $p_4 = 1 - m_3$, $v = (m_2 - 1)/(m_2 + 1)$, $m_i = \lambda_i/(\mu_i k)$.

According to (4), (9), and (18), the magnetic flux density in Region 5 can be obtained as follows:

$$B_{5x} = \frac{1}{4\pi^2}\int_{-\infty}^{\infty}\int_{-\infty}^{\infty}(C_{5ix} + C_{5rx})\,e^{-kz}e^{j(x\xi+y\eta)}d\xi d\eta \tag{24}$$

$$B_{5y} = \frac{1}{4\pi^2}\int_{-\infty}^{\infty}\int_{-\infty}^{\infty}(C_{5iy} + C_{5ry})\,e^{-kz}e^{j(x\xi+y\eta)}d\xi d\eta \tag{25}$$

$$B_{5z} = \frac{1}{4\pi^2}\int_{-\infty}^{\infty}\int_{-\infty}^{\infty}(C_{5iz} + C_{5rz})\,e^{-kz}e^{j(x\xi+y\eta)}d\xi d\eta \tag{26}$$

2.4. Spatial Frame Transformation Method

The process of an arbitrary spatial frame transformation can be divided into two steps: frame translation and frame rotation. Assuming that there are two spatial frames $\{o; \mathbf{e}_1, \mathbf{e}_2, \mathbf{e}_3\}$ and $\{o'; \mathbf{e}'_1, \mathbf{e}'_2, \mathbf{e}'_3\}$, their basis vectors are both standard orthonormal bases. The coordinates of the point P in these two frames are expressed as (x, y, z) and (x', y', z').

2.4.1. Frame Translation

As shown in Fig. 4, the frame $\{o'; \mathbf{e}'_1, \mathbf{e}'_2, \mathbf{e}'_3\}$ can be obtained by moving the origin of the frame $\{o; \mathbf{e}_1, \mathbf{e}_2, \mathbf{e}_3\}$ to o'. This process is called frame translation. Assuming that the coordinate of o' is $(\Delta x, \Delta y, \Delta z)$ in frame $\{o; \mathbf{e}_1, \mathbf{e}_2, \mathbf{e}_3\}$, (27) can be converted as follows:

$$\begin{bmatrix} x \\ y \\ z \end{bmatrix} = \begin{bmatrix} x' \\ y' \\ z' \end{bmatrix} + \begin{bmatrix} \Delta x \\ \Delta y \\ \Delta z \end{bmatrix} \tag{27}$$

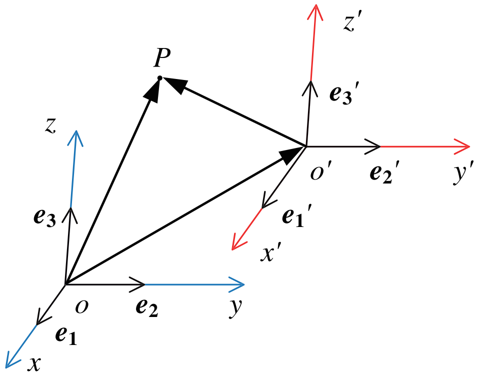

Figure 4. Schematic of the frame translation.

2.4.2. Frame Rotation

As shown in Fig. 5, frame $\{o; \mathbf{e}_1, \mathbf{e}_2, \mathbf{e}_3\}$ and frame $\{o'; \mathbf{e}'_1, \mathbf{e}'_2, \mathbf{e}'_3\}$ have the same origin and share one basis vector $(e_3 = e'_3)$. In addition, the angle between e_1 and e'_1 is equal to θ.

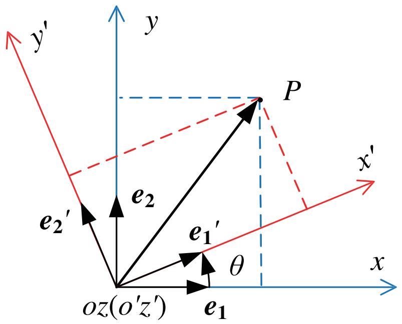

Figure 5. Schematic of the frame rotation.

According to Fig. 5, the Z-frame rotation formula can be obtained as (28).

$$\begin{bmatrix} x \\ y \\ z \end{bmatrix} = \begin{bmatrix} \cos\theta & -\sin\theta & 0 \\ \sin\theta & \cos\theta & 0 \\ 0 & 0 & 1 \end{bmatrix} \begin{bmatrix} x' \\ y' \\ z' \end{bmatrix} = E_Z \begin{bmatrix} x' \\ y' \\ z' \end{bmatrix} \tag{28}$$

Similarly, the frame transformation matrix of the X-frame rotation and Y-frame rotation are obtained as follows.

$$E_X = \begin{bmatrix} 1 & 0 & 0 \\ 0 & \cos\psi & -\sin\psi \\ 0 & \sin\psi & \cos\psi \end{bmatrix} \tag{29}$$

$$E_Y = \begin{bmatrix} \cos\varphi & 0 & \sin\varphi \\ 0 & 1 & 0 \\ -\sin\varphi & 0 & \cos\varphi \end{bmatrix} \tag{30}$$

2.4.3. General Spatial Frame Transformation

Frame translation and three kinds of frame rotations are considered to obtain the general frame transformation formula. Assuming that the deflection order around the axis from the original frames to the new frames is that X-axis is the first, Y-axis the second, and Z-axis the last, the relationship between coordinates of point P in these two frames can be expressed as follows:

$$\begin{bmatrix} x \\ y \\ z \end{bmatrix} = E_X E_Y E_Z \begin{bmatrix} x' \\ y' \\ z' \end{bmatrix} + \begin{bmatrix} \Delta x \\ \Delta y \\ \Delta z \end{bmatrix} = \begin{bmatrix} e_{11} & e_{12} & e_{13} \\ e_{21} & e_{22} & e_{23} \\ e_{31} & e_{32} & e_{33} \end{bmatrix} \begin{bmatrix} x' \\ y' \\ z' \end{bmatrix} + \begin{bmatrix} \Delta x \\ \Delta y \\ \Delta z \end{bmatrix} \tag{31}$$

2.5. Mutual Inductance Between Arbitrarily Placed Rectangular Coils

In this section, the mutual inductance formula of arbitrarily placed rectangular coils with double magnetic shielding is obtained based on the mathematical model of magnetic flux density and rotations transformation formula.

The mutual inductance between two coils can be expressed as follows [36]:

$$M = \frac{1}{I} \iint B \cdot ds \tag{32}$$

where s is the area surrounded by the receiving coil, and I is the current of the transmitting coil.

The expressions of the magnetic induction density in the new frame are obtained by combining (24)–(26) and (31).

$$B_{5x} = \frac{1}{4\pi^2} \int_{-\infty}^{\infty} \int_{-\infty}^{\infty} (C_{5ix} + C_{5rx}) e^{-k(e_{31}x' + e_{32}y' + e_{33}s_2 + \Delta z)} e^{j[(e_{11}x' + e_{12}y' + e_{13}s_2 + \Delta x)\xi + (e_{21}x' + e_{22}y' + e_{23}s_2 + \Delta y)\eta]} d\xi d\eta \tag{33}$$

$$B_{5y} = \frac{1}{4\pi^2} \int_{-\infty}^{\infty} \int_{-\infty}^{\infty} (C_{5iy} + C_{5ry}) e^{-k(e_{31}x' + e_{32}y' + e_{33}s_2 + \Delta z)} e^{j[(e_{11}x' + e_{12}y' + e_{13}s_2 + \Delta x)\xi + (e_{21}x' + e_{22}y' + e_{23}s_2 + \Delta y)\eta]} d\xi d\eta \tag{34}$$

$$B_{5z} = \frac{1}{4\pi^2} \int_{-\infty}^{\infty} \int_{-\infty}^{\infty} (C_{5iz} + C_{5rz}) e^{-k(e_{31}x' + e_{32}y' + e_{33}s_2 + \Delta z)} e^{j[(e_{11}x' + e_{12}y' + e_{13}s_2 + \Delta x)\xi + (e_{21}x' + e_{22}y' + e_{23}s_2 + \Delta y)\eta]} d\xi d\eta \tag{35}$$

According to (32)–(35), the mutual inductance expression of the single-turn rectangular coils is as follows:

$$M = \frac{1}{I} \int_{-b_1}^{b_1} \int_{-b_2}^{b_2} (B_{5x} + B_{5y} + B_{5z}) dx' dy' \tag{36}$$

In particular, when $t_2 = 0$, $\mu_2 = 1$, and .$\sigma_2 = 0$, (36) can be transformed into a calculation formula for mutual inductance of a rectangular coil with a single-layer magnetic shielding.

For multi-turn spiral coils, several concentric filamentary turns are used as equivalents of the spiral coils. According to the superposition principle, the total mutual inductance between the transmitting coil and receiving coil can be calculated by summing the mutual inductance values between every turn on one coil and all of the turns on the other coils.

$$M_{total} = \sum_{m=1}^{N_T} \sum_{n=1}^{N_R} M_{mn} \tag{37}$$

where N_T and N_R are the numbers of turns of the transmitting coil and receiving coil, respectively, and M_{mn} is the mutual inductance between the m-th turn of the transmitting coil and the n-th turn of the receiving coil.

2.6. Coupling Coefficient

Coupling coefficient, indicating the coupling degree of elements, is defined as follows:

$$k_{TR} = \frac{M_{TR}}{\sqrt{L_T L_R}} \tag{38}$$

where M_{TR} is the mutual inductance between T_x and R_x; L_T is the self-inductance of T_x; L_R is the self-inductance of R_x.

Similarly, self-inductance of the single turn with a double-layer magnetic shielding is as follows:

$$L = \frac{1}{4\pi^2} \int_{-\infty}^{\infty} \int_{-\infty}^{\infty} \int_{-a_1}^{a_1} \int_{-a_2}^{a_2} (1 + Te^{-2kz}) q e^{j(x\xi + y\eta)} dx dy d\xi d\eta \tag{39}$$

where

$$q = \frac{-2}{\xi\eta} \mu_0 k \sin(\xi a_1) \sin(\eta a_2) \tag{40}$$

Self-inductance of the multi-turn includes self-inductance of each turn and mutual inductance between turns, which can be expressed as follows:

$$L_{total} = \sum_{m=1}^{N_s} \sum_{n=1}^{N_s} L_{mn} \tag{41}$$

where N_s is the number of turns of the spiral coil, when $m = n$; L_{mn} is the self-inductance of the m-th turn, when m is not equal to n; L_{mn} is the mutual inductance between the m-th turn and n-th turn.

3. VERIFICATION

To verify the correctness of the proposed calculation method, the finite element tool Ansys Maxwell 14.0 is used for simulation. A set of measurement platforms of coupling coefficient is built, and the coil parameters selected in the experiment are consistent with the simulation. The simulation model and experimental setup are shown in Fig. 6 and Fig. 7.

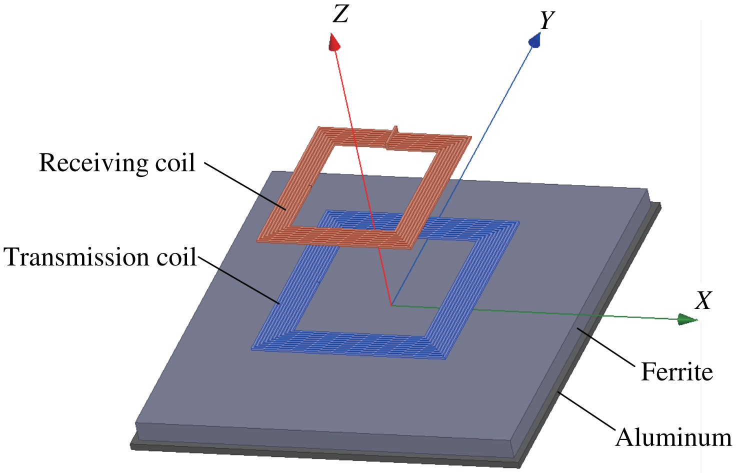

Figure 6. Simulation model diagram.

As shown in Fig. 7, the experimental values are obtained with the help of a TH2829A impedance analyzer, whose current frequency is 85 kHz. The measurement method of mutual inductance is as follows: When the transmitting coil is connected with the receiving coil in series, the measured inductance satisfies the equation $L_0 = L_T + L_R + 2M$; when the transmitting coil and receiving coil

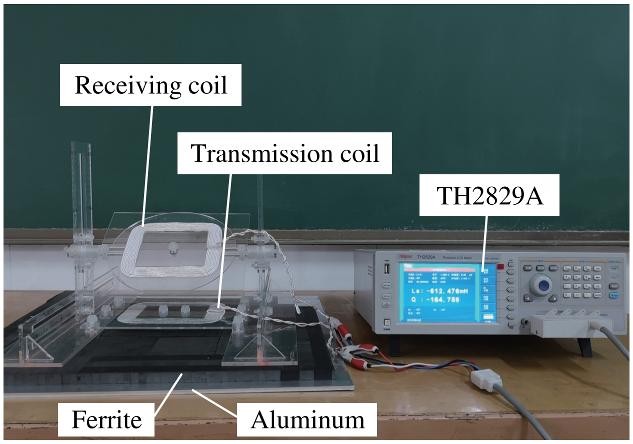

Figure 7. Diagram of experimental device.

Table 2. Parameters of coil and magnetic shields.

Symbol	Value
Innermost length of coils, a_1, b_1	120 mm
Innermost width of coils, a_2, b_2	100 mm
Number of turns of transmitting coil	12
Number of turns of receiving coil	10
Height of transmitting coil, s_1	17 mm
Height of receiving coil, s_2	100, 105 mm
Copper wire diameter	2 mm
Change of length and width	2.4 mm
Thickness of aluminum substrate, t_2	5 mm
Thickness of ferrite substrate, t_3	15 mm

are connected in reverse series, the measured inductance satisfies the equation $L_1 = L_T + L_R - 2M$. Therefore, the experimental values can be obtained according to $M = |L_0 - L_1|/4$. Here L_T is the self-inductance of the transmitting coil, and L_R is the self-inductance of the receiving coil. The parameters of the transmitting and receiving coils and magnetic tiles are shown in Table 2.

During the simulation and experiment, the transmitting coil and magnetic shielding are fixed, and the relative position is changed only by adjusting the coordinate of the receiving coil. The coupling coefficient of the coils at different positions is thereby modeled and analyzed. Considering the common position changes described in Section 1, six different cases are discussed in this section to validate the proposed formula, and the experimental model is shown in Fig. 8.

3.1. Vertical Distance Variation

The geometrical scheme of the coils with vertical distance variation is shown in Fig. 2(a). In this case, the distance variation along the Z-axis is defined as Δz, ranging from 0 mm to 100 mm with a step of 10 mm, and s_2 is equal to 100 mm. The calculated results (k_c), simulated results (k_s), and experimental results (k_e) of the coupling coefficient are presented in Table 3. In addition, the simulation error rates ε_1 and experiment error rates ε_2 are defined as follows:

$$\varepsilon_1 = |k_c - k_s|/k_s \tag{42}$$

$$\varepsilon_2 = |k_c - k_e|/k_e \tag{43}$$

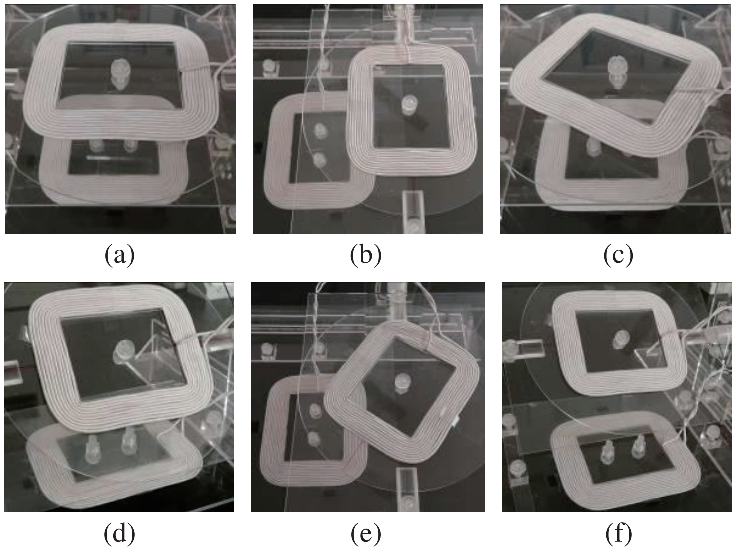

Figure 8. Experimental model of coil position variation (a) vertical distance variation, (b) horizontal misalignment, (c) horizontal angular misalignment, (d) vertical angular misalignment, (e) both horizontal angular and horizontal misalignment, (f) both vertical angular and horizontal misalignment.

Table 3. Coupling coefficient for vertical misalignment.

Δz/mm	k_c	k_s	k_e	ε_1	ε_2
0	0.1604	0.1626	0.1644	1.35%	2.43%
10	0.1357	0.1374	0.1392	1.24%	2.51%
20	0.1154	0.1171	0.1184	1.45%	2.53%
30	0.0987	0.0999	0.1005	1.20%	1.79%
40	0.0850	0.0860	0.0862	1.11%	1.34%
50	0.0734	0.0746	0.0749	1.61%	2.00%
60	0.0638	0.0647	0.0639	1.39%	0.16%
70	0.0558	0.0566	0.0562	1.41%	0.71%
80	0.0489	0.0496	0.0490	1.41%	0.20%
90	0.0431	0.0436	0.0429	1.15%	0.47%
100	0.0382	0.0386	0.0380	1.04%	0.53%

Table 3 shows that the simulation error rates ε_1 and experiment error rates ε_2 are not more than 2.53%. k_c is consistent with k_s and k_e, which validates the proposed formula in this case. In addition, Fig. 9 shows the corresponding graphical plot of the data in Table 3. The coupling coefficient value is maximal when Δz is minimal, and it gradually decreases with increasing distance due to the decrease in flux linkage.

3.2. Horizontal Misalignment

The geometrical scheme of the coils with horizontal misalignment is shown in Fig. 2(b). In this case, the horizontal misalignment along the X-axis is defined as Δx, which is ranged from 0 mm to 100 mm with a step of 10 mm, and s_2 is equal to 100 mm.

It is clearly seen from Table 4 that the simulation error rates are not more than 1.35%, and the experiment error rates are not more than 3.11% for horizontal misalignment. k_c, k_s, and k_e have

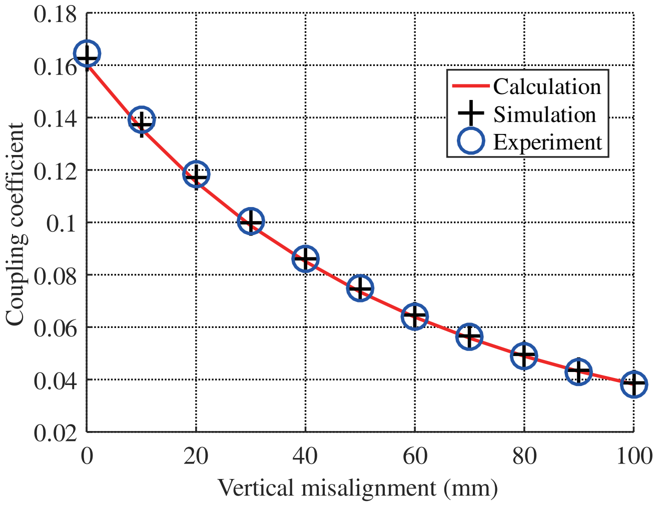

Figure 9. Diagram of the experimental results for vertical misalignment.

Table 4. Coupling coefficient for horizontal misalignment.

Δx/mm	k_c	k_s	k_e	ε_1	ε_2
0	0.1604	0.1626	0.1644	1.35%	2.43%
10	0.1589	0.1610	0.1620	1.30%	1.91%
20	0.1541	0.1561	0.1580	1.28%	2.47%
30	0.1464	0.1483	0.1511	1.28%	3.11%
40	0.1363	0.1380	0.1404	1.23%	2.92%
50	0.1243	0.1259	0.1282	1.27%	3.04%
60	0.1110	0.1122	0.1142	1.07%	2.80%
70	0.0969	0.0981	0.0998	1.22%	2.91%
80	0.0826	0.0835	0.0834	1.08%	0.96%
90	0.0686	0.0693	0.0687	1.01%	0.15%
100	0.0553	0.0558	0.0562	0.90%	1.60%

good consistency. Fig. 10 reflects the changes in the coupling coefficient obtained by the three analysis methods of calculation, simulation, and experiment as functions of the horizontal misalignment. The coupling coefficient is maximal when Δx is minimal, and it decreases gradually with increasing horizontal misalignment due to the flux linkage decrease.

3.3. Horizontal Angular Misalignment

The geometrical scheme of the coils with horizontal angular misalignment is shown in Fig. 2(c). Horizontal angular misalignment means that the receiving coil rotates an angle θ around the Z-axis. In this case, θ is ranged from 0° to 90° with a step of 10°, and s_2 is equal to 105 mm.

Table 5 shows that both the simulation error rates ε_1 and experiment error rates ε_2 are not more than 1.21% for horizontal angular misalignment. k_c is consistent with k_s and k_e. In this case, the changes in the coupling coefficient obtained by three analysis methods as functions of the angle are shown in Fig. 11. The coupling coefficient values are nearly constant as θ is ranged from 0° to 90°. This is because there are few changes in the area surrounded by the receiving coil during the rotation of this coil around the Z-axis.

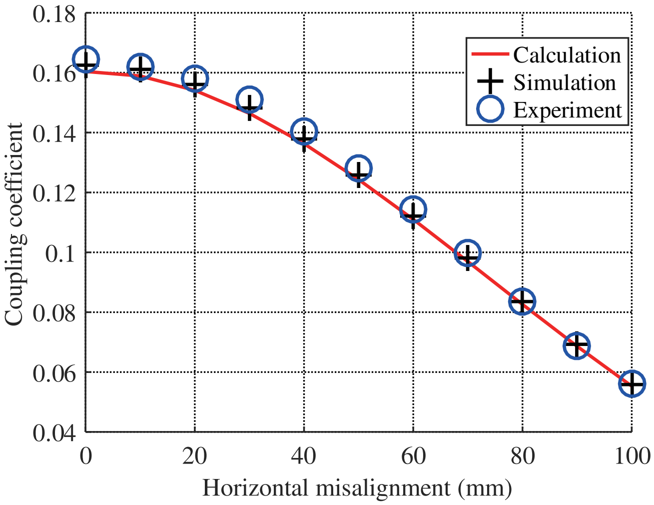

Figure 10. Diagram of the experimental results for horizontal misalignment.

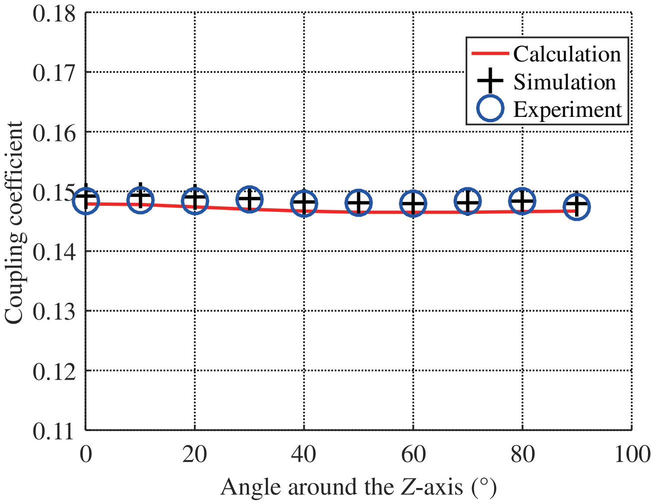

Figure 11. Diagram of the experimental results for horizontal deflection.

Table 5. Coupling coefficient for horizontal deflection.

$\theta/(^\circ)$	k_c	k_s	k_e	ε_1	ε_2
0	0.1479	0.1492	0.1483	0.87%	0.27%
10	0.1478	0.1493	0.1485	1.00%	0.47%
20	0.1474	0.1491	0.1484	1.14%	0.67%
30	0.1470	0.1488	0.1486	1.21%	1.08%
40	0.1467	0.1482	0.1480	1.01%	0.88%
50	0.1465	0.1481	0.1481	1.08%	1.08%
60	0.1465	0.1480	0.1480	1.01%	1.01%
70	0.1465	0.1481	0.1483	1.08%	1.21%
80	0.1466	0.1483	0.1483	1.13%	1.13%
90	0.1467	0.1480	0.1474	0.88%	0.47%

3.4. Vertical Angular Misalignment

The geometrical scheme of the coils with vertical angular misalignment is shown in Fig. 2(d). Vertical angular misalignment means that the receiving coil rotates an angle γ or around Y-axis. In this case, γ is ranged from 0° to 80° with a step of 10°, and s_2 is equal to 100 mm.

Table 6. Coupling coefficient for vertical deflection.

$\gamma/(^\circ)$	k_c	k_s	k_e	ε_1	ε_2
0	0.1604	0.1626	0.1644	1.35%	2.43%
10	0.1594	0.1635	0.1667	2.51%	4.38%
20	0.1617	0.1654	0.1691	2.24%	4.38%
30	0.1642	0.1671	0.1706	1.74%	3.75%
40	0.1643	0.1657	0.1695	0.84%	3.07%
50	0.1567	0.1569	0.1603	0.13%	2.25%
60	0.1350	0.1340	0.1350	0.75%	0.00%
70	0.0989	0.0970	0.0989	1.96%	0.00%
80	0.0521	0.0500	0.0545	4.18%	4.42%

According to Table 6, k_c, k_s, and k_e are in good agreement for vertical angular misalignment. Both simulation error rates ε_1 and experiment error rates ε_2 are not more than 4.42%. This is because the magnetic field is relatively scattered and uneven at the location of $\gamma = 80$. The graph of coupling coefficient obtained by the three analysis methods with the angle is shown in Fig. 12. Comparing Fig. 12 with Fig. 11, the changes in the coupling coefficient of the vertical angle misalignment are larger than those of the horizontal angle misalignment. The coupling coefficient values obtained by the three analysis methods are nearly constant as γ is ranged from 0° to 80°, and sharply decrease with a further increase in γ.

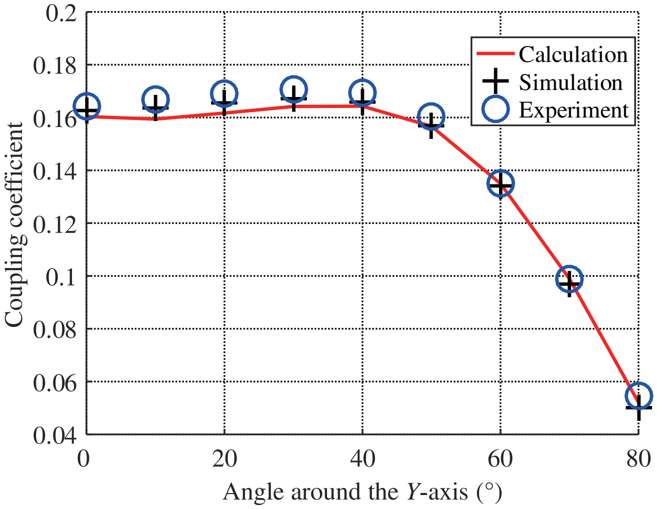

Figure 12. Diagram of the experimental results for vertical deflection.

3.5. Both Horizontal Angular and Horizontal Misalignments

The geometrical scheme of the coils with both horizontal angle and horizontal misalignment is shown in Fig. 2(e). In this case, the horizontal misalignment Δx is ranged from 0 mm to 100 mm with a step of 10 mm; the angle θ is 30° and 45°; and s_2 is equal to 105 mm.

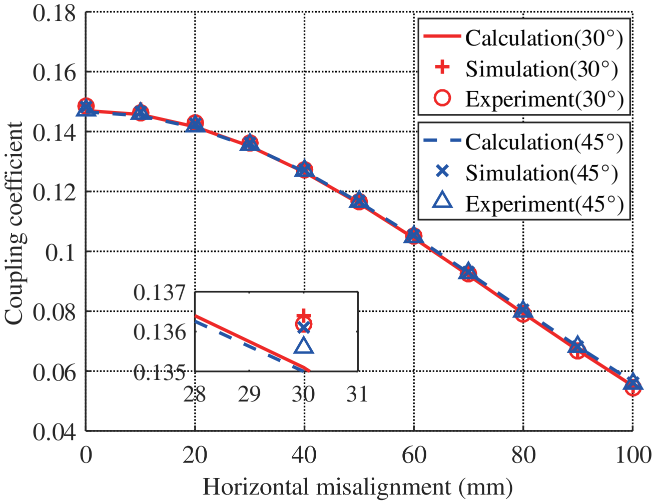

Figure 13. Diagram of the experimental results for Horizontal deflection with horizontal misalignment.

Table 7 shows that all simulation error rates ε_1 and experiment error rates ε_2 of both horizontal angle and horizontal misalignment are less than 2%. k_c, k_s, and k_e show great agreement. In addition, the graph of coupling coefficient obtained by the three analysis methods with horizontal misalignment is shown in Fig. 13, in which the curve of 30° basically coincides with the curve of 45°. The coupling coefficient value is at a maximum when the horizontal misalignment is minimal, and it rapidly decreases with increasing horizontal misalignment due to the decrease in flux linkage.

Table 7. Coupling coefficient for horizontal deflection with horizontal misalignment.

	$\theta = 30°$					$\theta = 45°$				
Δx/mm	k_c	k_s	k_e	ε_1	ε_2	k_c	k_s	k_e	ε_1	ε_2
0	0.1470	0.1488	0.1485	1.21%	1.01%	0.1466	0.1482	0.1472	1.08%	0.41%
10	0.1457	0.1473	0.1463	1.09%	0.41%	0.1453	0.1466	0.1459	0.89%	0.41%
20	0.1416	0.1429	0.1429	0.91%	0.91%	0.1413	0.1425	0.1418	0.84%	0.35%
30	0.1351	0.1364	0.1362	0.95%	0.81%	0.1350	0.1361	0.1356	0.81%	0.44%
40	0.1264	0.1275	0.1272	0.86%	0.63%	0.1266	0.1273	0.1269	0.55%	0.24%
50	0.1160	0.1168	0.1166	0.68%	0.51%	0.1164	0.1170	0.1167	0.51%	0.26%
60	0.1044	0.1050	0.1050	0.57%	0.57%	0.1050	0.1055	0.1047	0.47%	0.29%
70	0.0920	0.0924	0.0925	0.43%	0.54%	0.0928	0.0932	0.0927	0.43%	0.11%
80	0.0793	0.0796	0.0791	0.38%	0.25%	0.0804	0.0804	0.0798	0.00%	0.75%
90	0.0669	0.0670	0.0667	0.15%	0.30%	0.0681	0.0680	0.0680	0.15%	0.15%
100	0.0551	0.0549	0.0544	0.36%	1.29%	0.0565	0.0561	0.0558	0.71%	1.25%

3.6. Both Vertical Angular and Horizontal Misalignments

The geometrical scheme of the coils with both vertical angle and horizontal misalignment is shown in Fig. 2(f). In this case, the horizontal misalignment Δx is ranged from 0 mm to 100 mm with a step of 10 mm; the angle γ is 30° and 45°; and s_2 is equal to 100 mm.

Table 8 shows that all simulation error rates ε_1 and experiment error rates ε_2 of both vertical angle and horizontal misalignment are less than 4%. k_c, k_s, and k_e have good consistency. The corresponding line graph of the data in Table 8 is shown in Fig. 14. When the vertical angle is 30°, the coupling coefficient value reaches the maximum at the horizontal misalignment of −10 mm; when the deflection

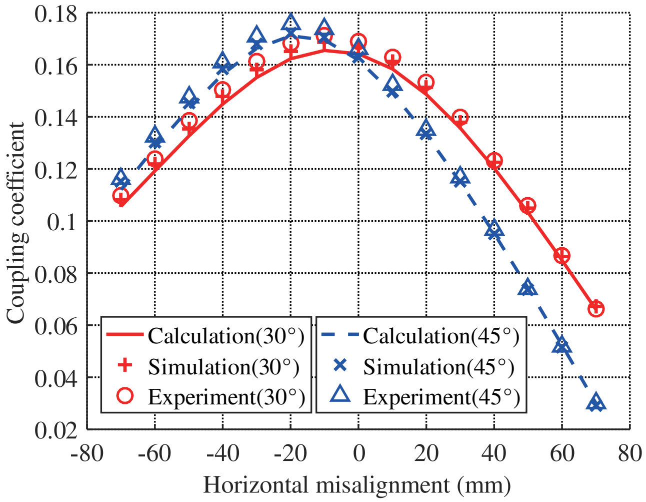

Figure 14. Diagram of the experimental results for vertical deflection with horizontal misalignment.

Table 8. Coupling coefficient for vertical deflection with horizontal misalignment.

	$\gamma = 30^\circ$					$\gamma = 45^\circ$				
Δx/mm	k_c	k_s	k_e	ε_1	ε_2	k_c	k_s	k_e	ε_1	ε_2
-70	0.1056	0.1081	0.1098	2.31%	3.83%	0.1120	0.1151	0.1163	2.69%	3.70%
-60	0.1192	0.1220	0.1239	2.30%	3.79%	0.1283	0.1301	0.1324	1.38%	3.10%
-50	0.1326	0.1355	0.1385	2.14%	4.26%	0.1431	0.1452	0.1474	1.45%	2.92%
-40	0.1449	0.1478	0.1505	1.96%	3.72%	0.1564	0.1583	0.1609	1.20%	2.80%
-30	0.1551	0.1582	0.1614	1.96%	3.90%	0.1663	0.1680	0.1710	1.01%	2.75%
-20	0.1623	0.1652	0.1684	1.76%	3.62%	0.1711	0.1723	0.1758	0.70%	2.67%
-10	0.1655	0.1685	0.1713	1.78%	3.39%	0.1695	0.1705	0.1737	0.59%	2.42%
0	0.1642	0.1671	0.1691	1.74%	2.90%	0.1618	0.1630	0.1661	0.74%	2.59%
10	0.1584	0.1612	0.1628	1.74%	2.70%	0.1492	0.1496	0.1524	0.27%	2.10%
20	0.1486	0.1513	0.1532	1.78%	3.00%	0.1332	0.1333	0.1352	0.08%	1.48%
30	0.1357	0.1380	0.1397	1.67%	2.86%	0.1149	0.1151	0.1167	0.17%	1.54%
40	0.1203	0.1225	0.1233	1.80%	2.43%	0.0952	0.0949	0.0968	0.32%	1.65%
50	0.1032	0.1051	0.1059	1.81%	2.55%	0.0742	0.0737	0.0739	0.68%	0.41%
60	0.0849	0.0865	0.0866	1.85%	1.96%	0.0523	0.0515	0.0517	1.55%	1.16%
70	0.0660	0.0673	0.0663	1.93%	0.45%	0.0300	0.0292	0.0300	2.74%	0.00%

angle is 45°, the maximum coupling coefficient value is obtained at the horizontal misalignment of -20 mm.

In summary, the calculation results are consistent with the simulated and experimental results in six cases, including vertical distance variation, horizontal misalignment, horizontal angular misalignment, vertical angular misalignment, both horizontal angular and horizontal misalignments, and both vertical angular and horizontal misalignments; these results sufficiently verified the calculation formula of the coupling coefficient between spiral rectangular coils with double magnetic shielding. As shown in Tables 3 to 8, small errors are unavoidable, because the actual coils are not completely consistent with the calculation model and the simulation. The actual coils are connected to the TH2829A Impedance Analyzer by long terminals. Besides, the experimental measurements may have some errors, and the magnetic fields are influenced by the surrounding environment. Additionally, the comparisons between

Table 9. Comparison between the proposed model and the previous literature.

Literature	Coil type	Magnetic shield	Misalignment cases	Maximum error
[26]	Square coil	Air core	Both angular and horizontal misalignment	16.06%
[21]	Circular coil	Single layer magnetic shield	Both angular and horizontal misalignment	4.78%
[24]	Rectangular coil	Air core	Horizontal misalignment	10.63%
[30]	Rectangular coil	Single layer magnetic shield	Horizontal Misalignment	9.67%
[32]	Rectangular coil	Single layer magnetic shield	Horizontal Misalignment	15.00%
Proposed model	Rectangular coil	Double magnetic shield	Arbitrarily position	4.42%

other references and our work are shown in Table 9. Compared to [21, 24, 26, 30, 32], the error rate of the coupling coefficients in our work is minimal.

4. CONCLUSION

In this paper, a calculation method for the coupling coefficient based on dual Fourier transformation and spatial frame transformation method is proposed, by which the coupling coefficient between rectangular coils with six kinds of misalignments on a double magnetic shielding substrate is calculated without the time-consuming finite element simulation. In the model, the two coils can have different sizes, turn numbers, and positions, and magnetic shielding can be composed of one or two materials; thus, the calculation method proposed in this paper for coupling coefficient is more general than the previous methods. The results of the coupling coefficient obtained from the calculation are compared with those of simulation and experiment. All simulation error rates ε_1 and experiment error rates ε_2 are less than 5%, and the results of the three analysis methods have good consistency. This research provides a theoretical basis for the coil design and parameter optimization of a WPT system with double magnetic shielding and has reference significance for the future studies of coils between two double-layers or multilayer magnetic substrates.

ACKNOWLEDGMENT

This work was supported in part by the National Natural Science Foundation of China under Grant 11901188, in part by the Natural Science Foundation of Hunan Province under Grants 2019JJ60055 and 2022JJ30226, in part by the Outstanding Youth Project of Hunan Education Department under Grants 20B186 and 18A272.

REFERENCES

1. Liu, D., K. Zhou, Y. Liu, et al., "Research on constant output power based on double pick-up in dynamic wireless power transfer system," *Proceedings of the CSEE*, Vol. 39, No. 13, 3899–3907, 2019.
2. Huang, X., W. Wang, L. Tan, et al., "Technical progress and application development of magnetic coupling resonant wireless power transfer," *Automation of Electric Power Systems*, Vol. 41, No. 2, 2–14+141, 2017.
3. Jia, J. and X. Yan, "Research tends of magnetic coupling resonant wireless power transfer characteristics," *Transactions of China Electrotechnical Society*, Vol. 35, No. 20, 4217–4231, 2020.
4. Fan, X., X. Mo, X. Zhang, et al., "Research status and application of wireless power transmission technology," *Proceedings of the CSEE*, Vol. 35, No. 10, 2584–2600, 2015.

5. Xie, W. and W. Chen, "Research progress of omnidirectional wireless power transfer technology," *Automation of Electric Power Systems*, Vol. 44, No. 4, 202–221, 2020.
6. Yang, M., R. Mai, L. Xu, et al., "Coaxial phase detection coil and its application for dynamic resonance tuning in inductive wireless power transfer systems," *Proceedings of the CSEE*, Vol. 37, No. 6, 1867–1875, 2017.
7. Kou, Z., B. Yang, Y. Chen, et al., "Study on IPT charging system with the characteristics of misalignment tolerant in 2-dimensional plane and constant voltage output," *Proceedings of the CSEE*, Vol. 38, No. 15, 4576–4584+4658, 2018.
8. Wang, Y., K. Lu, Y. Yao, et al., "An electric vehicles (EV)-oriented wireless power transfer system featuring high misalignment tolerance," *Proceedings of the CSEE*, Vol. 39, No. 13, 3907–3917, 2019.
9. Chen, F., R. Mai, Y. Li, et al., "Efficiency optimization of three-coil structure WPT systems based on relay coil switching," *Proceedings of the CSEE*, Vol. 39, No. 21, 6373–6383, 2019.
10. Sun, Y., C. Jiang, Z. Wang, et al., "Optimal planning of dynamic wireless supply system for electric vehicles based on particle swarm genetic algorithm," *Automation of Electric Power Systems*, Vol. 43, No. 9, 125–133, 2019.
11. Mai, R., Y. Li, Z. He, et al, "Wireless power transfer technology and its research progress in rail transportation," *Journal of Southwest Jiaotong University*, Vol. 51, No. 3, 446–461, 2016.
12. Pratik, U., B. J. Varghese, A. Azad, et al., "Optimum design of decoupled concentric coils for operation in double-receiver wireless power transfer systems," *IEEE Journal of Emerging and Selected Topics in Power Electronics*, Vol. 7, No. 3, 1982–1998, 2019.
13. Yan, Z., B. Song, Y. Zhang, et al., "A rotation-free wireless power transfer system with stable output power and efficiency for autonomous underwater vehicles," *IEEE Transactions on Power Electronics*, Vol. 34, No. 5, 4005–4008, 2019.
14. Zhang, K., Y. Ma, Z. Yan, et al., "Eddy current loss and detuning effect of seawater on wireless power transfer," *IEEE Journal of Emerging and Selected Topics in Power Electronics*, Vol. 8, No. 1, 909–917, 2020.
15. Zhu, C., J. Jiang, K. Song, et al., "Research progress of key technologies for dynamic wireless charging of electric vehicle," *Automation of Electric Power Systems*, Vol. 41, No. 2, 60–65+72, 2017.
16. Li, R., Q. Yang, Y. Li, et al., "Efficient shielding design and optimization of wireless power transfer system with proximity coupling," *Automation of Electric Power Systems*, Vol. 43, No. 21, 163–171, 2019.
17. Cheng, S., "Progress in advanced electrical materials," *Proceedings of the CESS*, Vol. 37, No. 15, 4273–4285+4567, 2017.
18. Xu, Q., Y. Xu, and R. Mai, "IPT resonant reactive shielding systems with the characteristics of optimal magnetic shielding effect on target surface," *Proceedings of the CSEE*, Vol. 39, No. 18, 5490–5498+5597, 2019.
19. Jing, X., "Study on composite magnetic material structure in wireless power transmission system," *Qingdao University*, Qingdao, 2019.
20. Zhang, X., C. Quan, and Z. Li, "Mutual inductance calculation of circular coils for an arbitrary position with electromagnetic shielding in wireless power transfer systems," *IEEE Transactions on Transportation Electrification*, Vol. 7, No. 3, 1196–1204, 2021.
21. Li, Z. and M. Zhang, "Mutual inductance calculation of circular coils arbitrary positioned with magnetic tiles for wireless power transfer system," *IET Power Electronics*, Vol. 13, No. 16, 3522–3527, 2020.
22. Wu, D., T. He, X. Wang, et al., "Analytical modeling and analysis of mutual inductance coupling of rectangular spiral coils in inductive power transfer," *Transactions of China Electrotechnical Society*, Vol. 33, No. 3, 680–688, 2018.
23. Kuang, X. and L. Jia, "On the mutual induction coefficient and magnetic force between two coaxial rectangle coils carrying current," *Journal of China West Normal University (Natural Science)*, Vol. 38, No. 4, 426–429, 2017.

24. Oliveira, R. and P. Lehn, "An improved mutual inductance electromagnetic model for inductive power transfer systems under misalignment conditions," *IEEE Transactions on Vehicular Technology*, Vol. 69, No. 6, 6079–6093, 2020.
25. Misakian, M., "Equations for the magnetic field produced by one or more rectangular loops of wire in the same plane," *Journal of Research of the National Institute of Standards and Technology*, Vol. 105, No. 4, 557–564, 2000.
26. Joy, E. R., A. Dalal, and P. Kunar, "Accurate computation of mutual inductance of two air core square coils with lateral and angular misalignments in a flat planar surface," *IEEE Transactions on Magnetics*, Vol. 50, No. 1, 1–9, 2014.
27. Cheng, Y. and Y. Shu, "Mutual inductance calculation between arbitrarily positioned rectangular filaments," *International Journal of Applied Electromagnetics and Mechanics*, Vol. 46, No. 3, 287–298, 2014.
28. Liu, Y. and S. He, "The calculation of mutual inductance of two polygons with multiturn coils at arbitrarily position," *Value engineering*, Vol. 32, No. 31, 235–237, 2013.
29. Itaya, T., K. Ishida, A. Tanaka, et al., "Eddy current distribution for a rectangular coil arranged parallel to a moving conductor slab," *IET Science, Measurement & Technology*, Vol. 6, No. 2, 43–51, 2012.
30. Hao, K., S. Huang, W. Zhao, et al., "Analytical modelling and calculation of impedance and pulsed magnetic field for rectangular meander coil based on second order potential," *Acta Physica Sinica*, Vol. 60, No. 7, 791–800, 2011.
31. Smeets, J. P. C., T. T. Overboom, J. W. Jansen, et al., "Mode-matching technique applied to three-dimensional magnetic field modeling," *IEEE Transactions on Magnetics*, Vol. 48, No. 11, 3383–2286, 2012.
32. Luo, Z. and X. Wei, "Analysis of square and circular planar spiral coils in wireless power transfer system for electric vehicles," *IEEE Transactions on Industrial Electronics*, Vol. 65, No. 1, 331–341, 2018.
33. Kushwaha, B. K., G. Rituraj, and P. Kumar, "3-D analytical model for computation of mutual inductance for different misalignments with shielding in wireless power transfer system," *IEEE Transactions on Transportation Electrification*, Vol. 3, No. 2, 332–342, 2017.
34. Wu, L., K. Lu, and Y. Xia, "Mutual inductance calculation of two coaxial solenoid coils with iron core," *2018 21st International Conference on Electrical Machines and Systems (ICEMS)*, Jeju, Korea, 2018.
35. Cui, X., "Magnetic field and inductance of filament conductor segment model with current continuity," *Acta Physica Sinica*, Vol. 69, No. 3, 93–104, 2020.
36. Piri, M., V. Jaros, and M. Frivaldsky, "Verification of a mutual inductance calculation between two helical coils," *2015 16th International Scientific Conference on Electric Power Engineering (EPE)*, Kouty nad Desnou, Czech Republic, 2015.